

Electronic Supplementary Information

Constructing n/n⁺ homojunction in monolithic perovskite film for boosting charge collection in inverted perovskite photovoltaics

*Yan-Na Lu^{a†}, Jun-Xing Zhong^{a†}, Yinye Yu^{cf}, Xi Chen^a, Chan-Ying Yao^a, Chengxi Zhang^b, Meifang Yang^a, Wenhui Feng^a, Yong Jiang^e, Ying Tan^a, Li Gong^d, Xingzhan Wei^f, Yecheng Zhou^{*c}, Lianzhou Wang^{*b} and Wu-Qiang Wu^{*a}*

[†]Equally contributed to this work

^a MOE Key Laboratory of Bioinorganic and Synthetic Chemistry, Lehn Institute of Functional Materials, School of Chemistry, Sun Yat-sen University, Guangzhou 510275, P R China

*Email: wuwq36@mail.sysu.edu.cn

^b Nanomaterials Centre, School of Chemical Engineering and Australian Institute for Bioengineering and Nanotechnology, The University of Queensland, Brisbane, QLD 4072, Australia.

*Email: l.wang@uq.edu.au

^c School of Materials Science & Engineering, Sun Yat-sen University, Guangzhou 510275, P R China

*Email: zhouych29@mail.sysu.edu.cn

^d Instrumental Analysis Research Center, Sun Yat-sen University, Guangzhou 510275, P R China

^e College of Biological and Chemical Engineering, Guangxi University of Science and Technology, Liuzhou 545006, P R China

^f Micro-nano manufacturing and system integration center, Chongqing Institute of Green and Intelligent Technology, Chinese Academy of Sciences, Chongqing 400714, P R China

Defect Chemistry Calculation:

First-principles calculations were performed to investigate the possible doping effect brought about by InBr_3 treatment on the perovskite surface. Density Function Theory (DFT) calculations were carried out with the Vienna Ab-initio Simulation Package (VASP 5.4.4),(1, 2) which implemented a projector augmented-wave (PAW) method(3) using a plane-wave basis set. The exchange correlation was calculated using the Perdew-Burke-Ernzerhof exchange-correlation functional as revised for solids (PBEsol),(4) which gave the most accurate lattice constant in our previous work.(5) The generalized gradient approximation (GGA) PBEsol calculations were done with the PBE-PAW potential considering 14 valence electrons: $5d^{10}6s^26p^2$, $5s^25p^2$, $2s^22p^2$, $2s^22p^3$ and $1s$ for lead, iodine, carbon, nitrogen and hydrogen, respectively. An energy cut-off of 550 eV was used. Defect calculation details can be found in our previous work.(6)

Defect models:

Defect models were prepared according to reference (7).

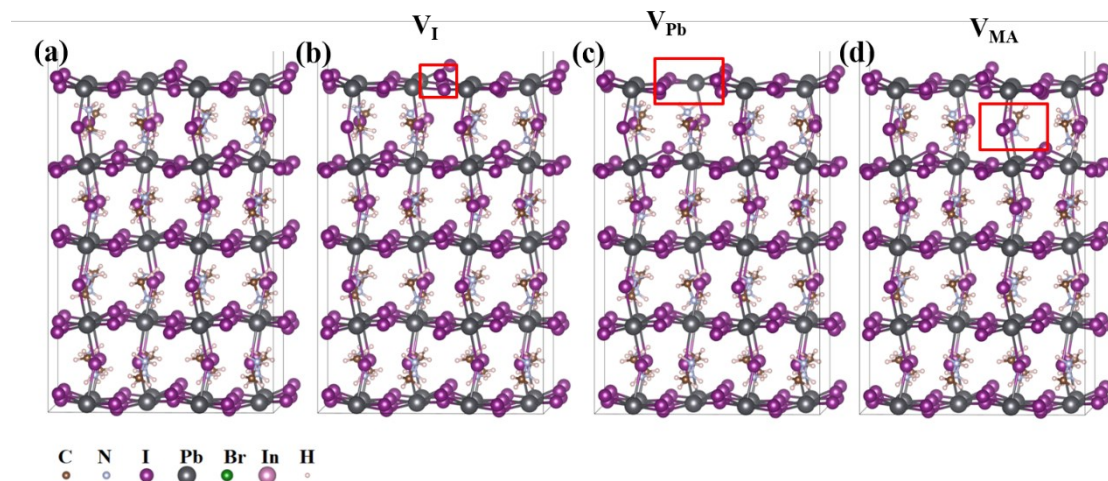


Fig. S1. Structures of the (a) intrinsic surface, (b) surface with a I vacancy, (c) surface with a Pb vacancy, and (d) surface with a MA vacancy.

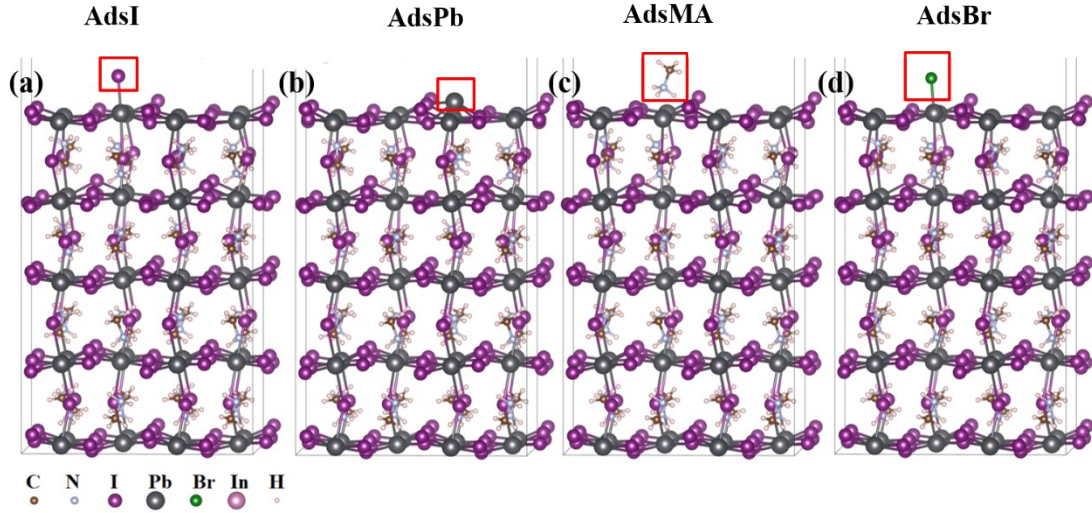


Fig. S2. Structures of the surface with one (a) I, (b) Pb, (c) MA or (d) Br adsorbed.

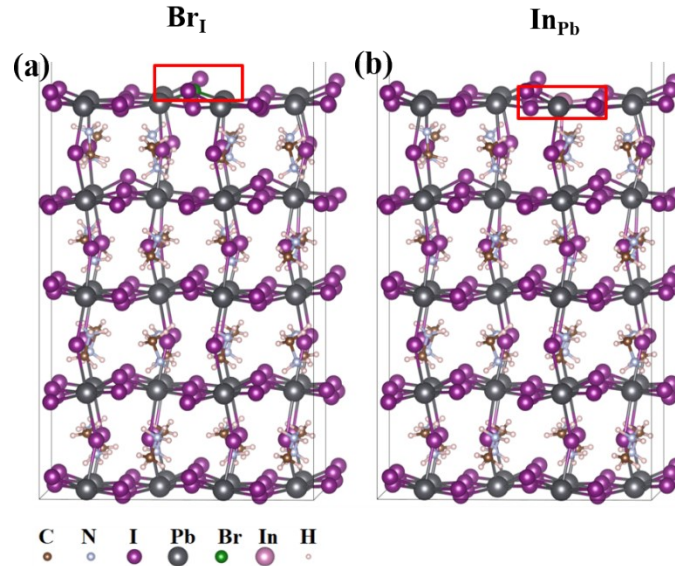


Fig. S3. (a) The surface with a substitutional Br at the I site, and (b) the surface with a substitutional In on the Pb site.

Formation energy:

Formation energies were calculated based on the total energy of defects.

$$\begin{aligned} \Delta H_f(\alpha, q) = & E(\alpha, q) - E(\text{host}) + \sum_i n_i (E_i + \mu_i) \\ & + q[\varepsilon_{\text{VBM}}(\text{host}) + E_F], \end{aligned} \quad (2)$$

As the perovskite thin films were fabricated with slightly excessive PbI_2 , the surface vacancies of Pb and I, and surface adsorption of MA were not considered. Fig. S4 shows the Fermi level

dependent defect formation energies without InBr_3 doping. It was found that the formation energy of the MA vacancy is less than 1.0 eV, which thus should be the dominant surface defect. The negative MA vacancy indicates that the intrinsic perovskite become p-type with excessive PbI_2 . The formation energies of surface adsorbed iodine and lead are higher, but both are possible to occur at room temperature.

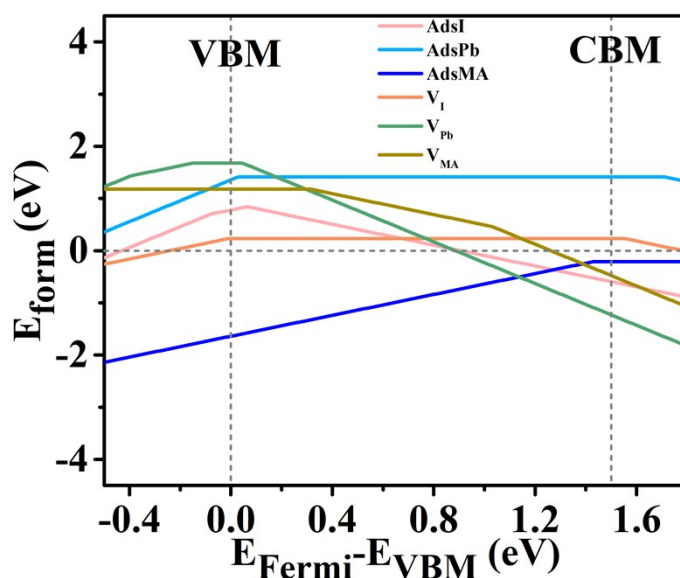


Fig. S4. Formation energies of intrinsic surface point defects. AdsI, AdsPb and AdsMA represent adsorbed I, Pb and MA, respectively. V_I , V_{Pb} and V_{MA} represent I, Pb and MA vacancies, respectively.

Work function calculations

The work functions of these defect models were calculated. Figure S5 shows the summation of local potential of defects along the Z axis, which gives the vacuum level of the slabs. By calculating the energy difference between the Fermi and vacuum levels, the work function is obtained (Table S1). Since the DFT calculations are based on the ferroelectric surface, a large dipole moment exists. The work functions of the bottom and top surfaces are not the same. Here, we used the average work function of the top and bottom surfaces to eliminate any effect from possible ferroelectric polarization. The most populated defect of Br_1 slightly increased the work function by less than 0.01

eV. However, the second populated defect (In_{Pb}) significantly decreases the work function by more than 0.3eV. The complex defect with three In_{Pb} and one Br_{I} also decreased the work function by more than 0.3eV. Hence, the work function change of the perovskite film is largely dominated by In_{Pb} defects.

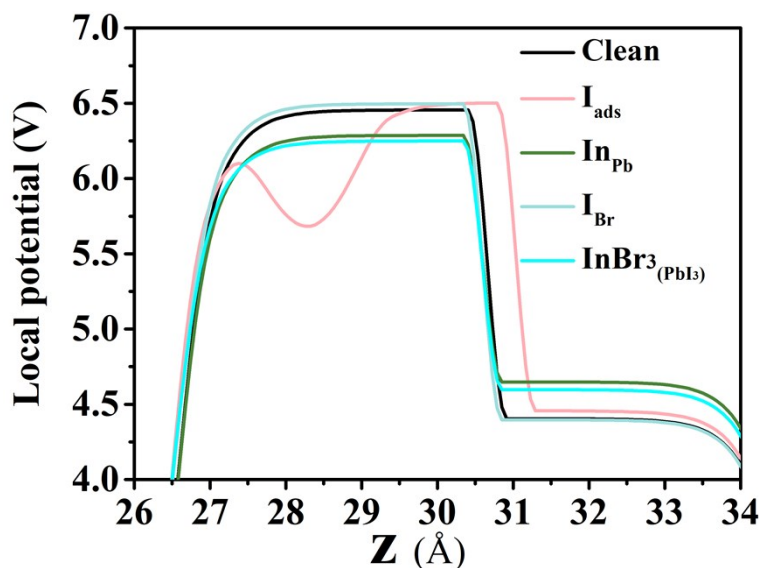


Fig. S5. Local potential of surface in the vacuum layer of doped perovskite slabs with various defects. The stage in the figure is produced by dipole correction, because the two surfaces of slab are not the same.

Table S1. Calculated Fermi energy level, vacuum level and work functions of doped and undoped surfaces.

Surface	E-Fermi (eV)	Vacuum level of top/bottom surfaces (eV)	Average work function (eV)
Intrinsic surface	0.64	6.47/4.40	4.79
Br_{I}	0.64	6.50/4.40	4.80
In_{Pb}	1.00	6.29/4.65	4.46
$\text{InBr}_3(\text{PbI}_3)$	0.95	6.25/4.60	4.47

In conclusion, both the defect formation calculations and the work function calculations show that surface treatment of perovskite films by InBr_3 will increase the concentration of electrons, lift the work function and induce a surface n-type doping effect.

Table S2. The main parameters for device simulation. Note, the values shown in brackets are specific for the InBr_3 -doped perovskite, otherwise they are targeted for the undoped perovskite.

Materials	PTAA	CFM	C₆₀
Density of states of the conduction band N_c (cm⁻³)	2×10^{18}	5×10^{18}	2×10^{18}
Density of states of the valence band N_v (cm⁻³)	2×10^{18}	5×10^{18}	2×10^{18}
Concentration of donor-like defects N_d (cm⁻³)	0.00	7×10^{15} (2.5×10^{18})	1.3×10^{18}
Concentration of acceptor-like defects N_a (cm⁻³)	1.3×10^{18}	0.00	0.00
Relative Permittivity	3.00	5.00	5.00
Band gap E_g (eV)	3.35	1.51	1.74
Electron Affinity (eV)	1.90	4.19 (4.28)	4.50
Mobility (μ_n, cm²/V·s)	0.01	1.00	0.006
Mobility (μ_p, cm²/V·s)	0.01	1.00	0.006
Defect energy level (eV)	1.75	0.75	0.85
Capture rate n (cm²)	10^{-10}	0.5×10^{-15}	10^{-10}
Capture rate p (cm²)	10^{-10}	0.5×10^{-15}	10^{-10}
Defect density (cm⁻³)	10^{15}	0.95×10^{15}	10^{15}

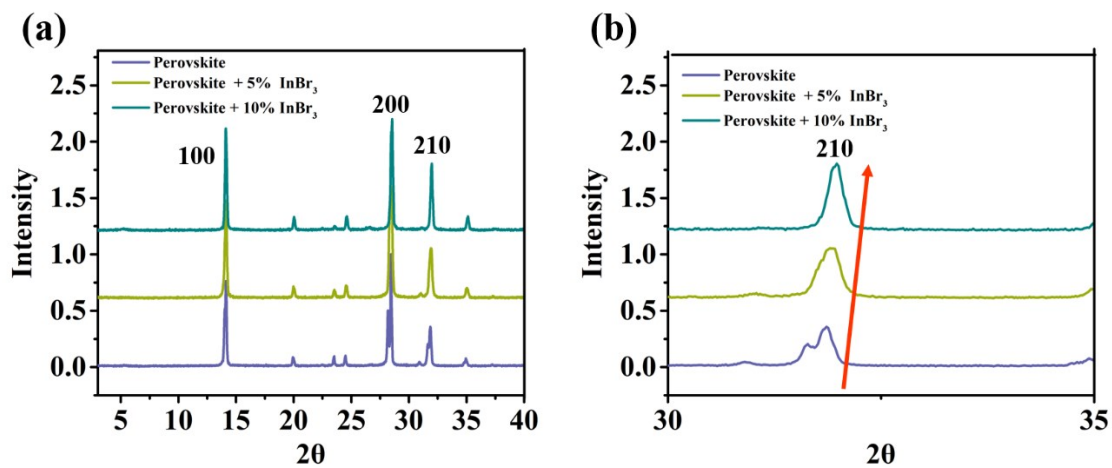


Fig. S6. (a) XRD patterns of the perovskite crystals incorporating different amounts of InBr₃. (b) Enlarged view showing the shift of the (210) characteristic peak.

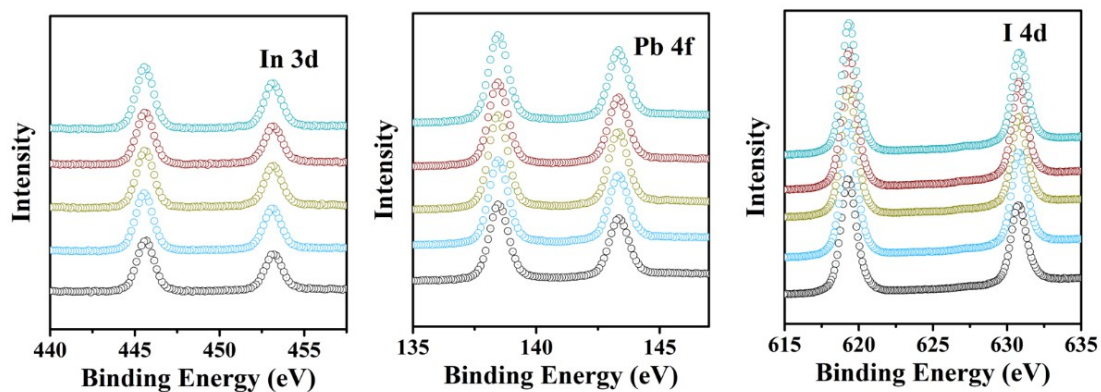


Fig. S7. High resolution XPS spectra of (a) In, (b) Pb and (c) I in five selected surface regions of InBr₃-treated perovskite film.

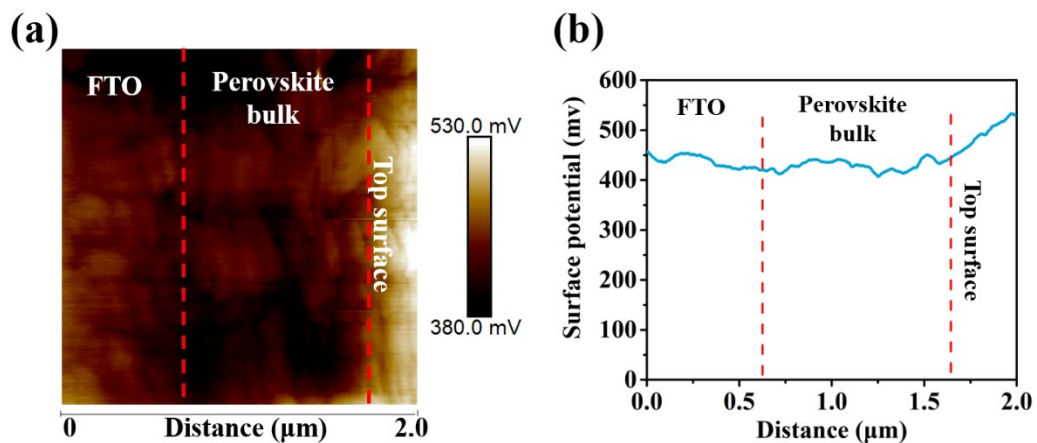


Fig. S8. Cross-sectional KPFM measurements for InBr_3 -treated perovskite film deposited on FTO glass: (a) potential mapping and (b) line profiles of surface potential.

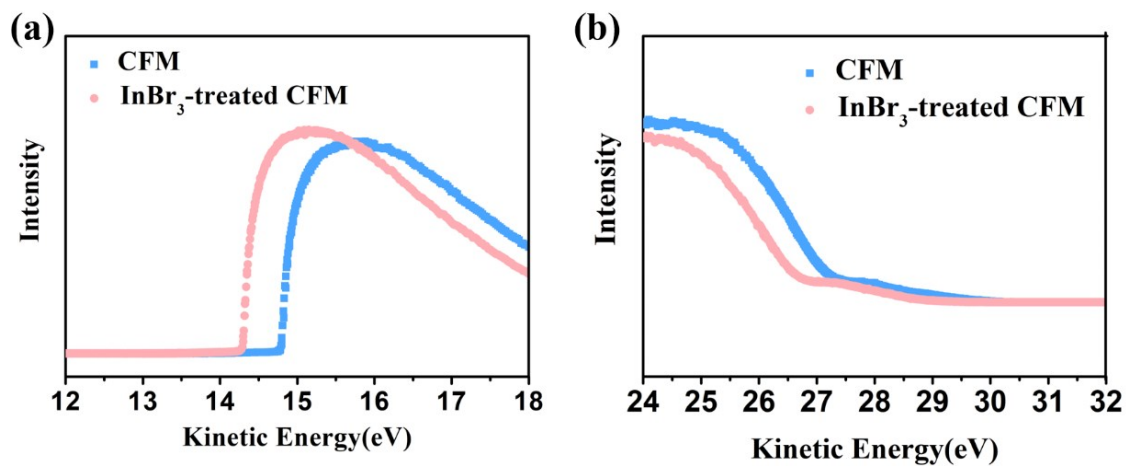


Fig. S9. (a) Secondary electron cut-off and (b) valence band spectra of CFM and InBr_3 -treated CFM films from UPS measurements.

Table S3. Summarized decay lifetime for samples based on CFM and InBr₃-treated CFM perovskite films. Note, the values were extracted from the dynamic TA measurement in Fig. 3i.

	A ₁	τ ₁	A ₂	τ ₂	A ₃	τ ₃	A ₄	T ₄	average
	(%)	(ps)	(%)	(ps)	(%)	(ps)	(%)	(ps)	(ps)
CFM	50.1	1.33	20.3	52.3	25.6	284	4.0	N/A	252
InBr ₃ -treated CFM	40.7	1.02	10.0	6.62	43.9	52.3	5.4	N/A	50

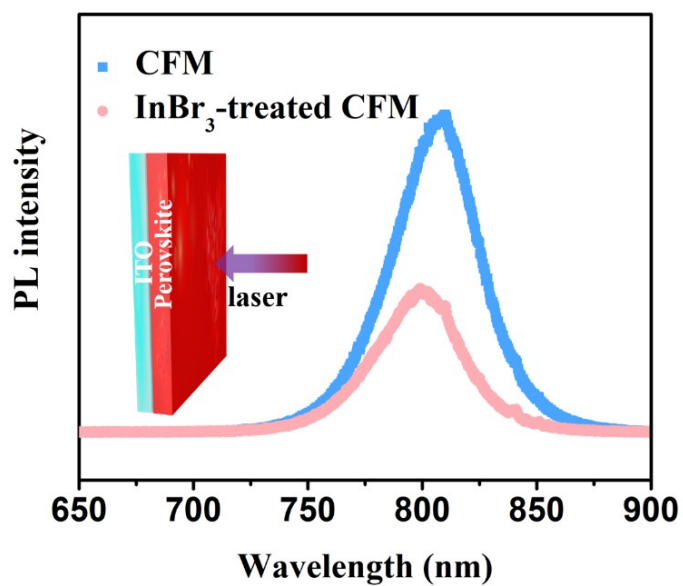


Fig. S10. Steady-state PL intensity of ITO/perovskite samples based on CFM and InBr₃-treated CFM films.

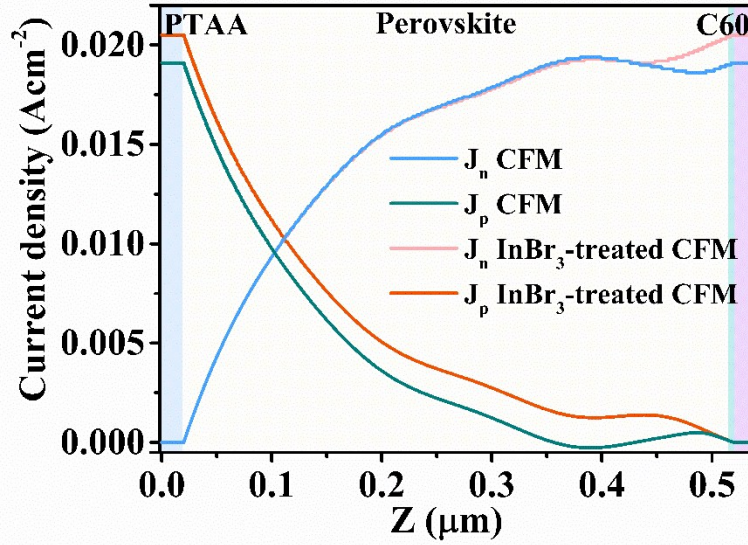


Fig. S11. The calculated electron current density (J_n) and hole current density (J_p) of analog devices with or without InBr_3 treatment at a bias of 1.0 V.

In the device simulation, the electron and hole currents were generated by the movement of accumulated charge carriers from one electrode to the opposite side. Specifically, the electron current starts from PTAA side, and gradually become larger toward the right side owing to the movement of electrons from PTAA to C60 side. The electron current can be calculated according to the following equation: $J_{Z+\Delta Z} = J_Z + \Delta J_Z$, where ΔJ_Z is the current produced by the moving electrons in the region of ΔZ . As the device parameters on the left side of homojunction region are similar for both the control and target group, the electron current should be similar. Near the homojunction region, the target ΔJ_Z is higher than the control group, so that the electron current will be larger for the former. Hence, the electron current density is only significantly different on the side near the ETL, which also verified the formation of n/n^+ homojunction near the perovskite/ETL interface. In contrast, the hole current starts from the right side, which can be calculated by the following equation: $J_{Z-\Delta Z} = J_Z + \Delta J_Z$. At the C_{60} side, no hole current is generated. With decreased Z , the hole current become larger. Near the homojunction region, holes move faster for the target group due to the built-in electric field, leading to a higher hole current than the control group. Beyond the homojunction region, the local current increasing are similar for the control and the target group ($\Delta J_Z(\text{exp}) = \Delta J_Z(\text{control})$). Considering the total current at $Z-\Delta Z$ of target

device ($J_{Z-\Delta Z}(\text{exp}) = J_z(\text{exp}) + \Delta J_z(\text{exp})$) is higher than the control device ($J_{Z-\Delta Z}(\text{control}) = J_z(\text{control}) + \Delta J_z(\text{control})$), after deducting the similar electron current at these regions, we interpreted that the hole current for target device is higher than its control counterpart.

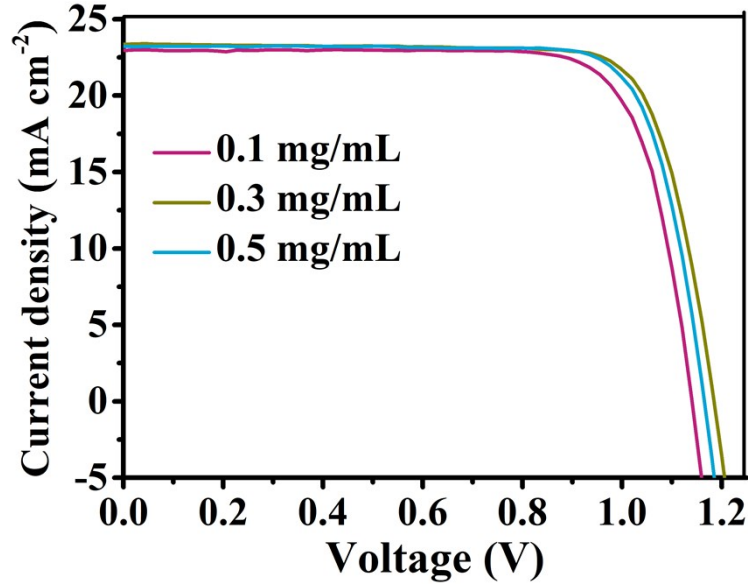


Fig. S12. J - V curves of the PSCs based on the perovskite films treated with different concentrations of InBr_3 .

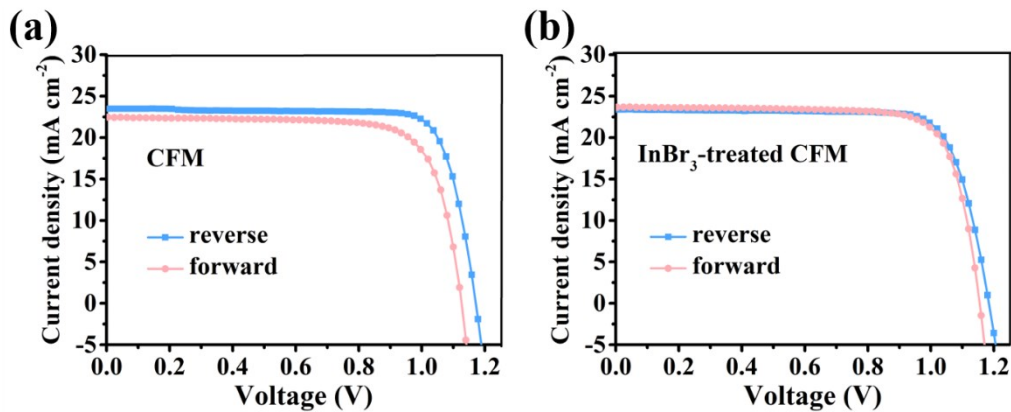


Fig. S13. J - V curves of the PSCs based on different perovskite films measured under forward and reverse scanning directions: (a) CFM and (b) InBr_3 -treated CFM.

Table S4. Photovoltaic parameters of the PSC based on CFM or InBr₃-treated CFM perovskite films measured under AM 1.5 G illumination at forward and reverse scanning directions.

PSCs	Scan direction	J_{SC} (mA cm ⁻²)	V_{OC} (V)	η (%)	FF (%)
InBr ₃ -treated CFM	forward	23.7	1.16	21.4	0.78
	reverse	23.4	1.18	21.8	0.79
CFM	forward	22.3	1.10	18.1	0.73
	reverse	22.5	1.12	19.2	0.76

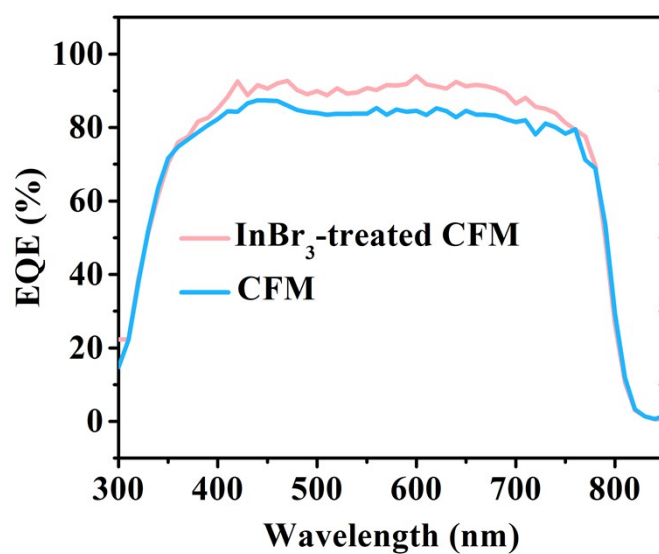


Fig. S14. EQE spectra of the PSC based on the CFM and InBr₃-treated CFM film.

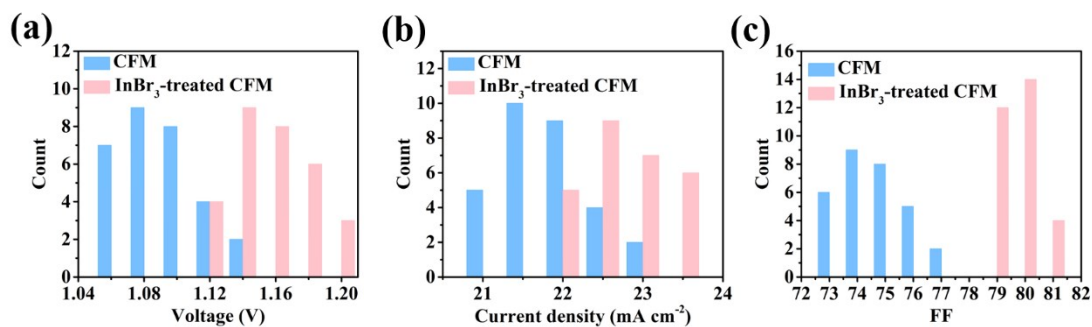


Fig. S15. V_{OC} , J_{SC} , FF histograms of the PSCs based on CFM and InBr₃-treated CFM films.

Reference

1. G. Kresse and J. Furthmüller, *Comput. Mater. Sci.* 1996, **6**, 15-50.
2. G. Kresse and J. Furthmüller, *Phys. Rev. B*, 1996, **54**, 11169-11186.
3. P. E. Blöchl, *Phys. Rev. B*, 1994, **50**, 17953-17979.
4. J. P. Perdew, A. Ruzsinszky, G. I. Csonka, O. A. Vydrov, G. E. Scuseria, L. A. Constantin, X. Zhou and K. Burke, *Phys. Rev. Lett.* 2008, **100**, 136406.
5. Y. Zhou, F. Huang, Y.-B. Cheng and A. Gray-Weale, *Phys. Chem. Chem. Phys.*, 2015, **17**, 22604-22615.
6. T. Feng and X. Ruan, *Phys. Rev. B*. 2018, **97**, 045202.
7. H. Uratani and K. Yamashita, *The Journal of Phys. Rev. Lett.* 2017, **8**, 742-746.